Targeting a G-quadruplex from let-7e pre-miRNA with small molecules and nucleolin

Tiago Santos, André Miranda, Lionel Imbert, David Monchaud, Gilmar Salgado, Eurico Cabrita, Carla Cruz

Targeting a G-quadruplex from let-7e pre-miRNA with small molecules and nucleolin

Tiago Santos [1], André Miranda [1], Lionel Imbert [2,3], David Monchaud [4], Gilmar F. Salgado [5], Eurico J. Cabrita [6,7] and Carla Cruz [1]*

[1] CICS-UBI - Centro de Investigação em Ciências da Saúde, Universidade da Beira Interior, Av. Infante D. Hen-rique, 6200-506, Covilhã, Portugal;

[2] Univ. Grenoble Alpes, CNRS, CEA, Institut de Biologie Structurale (IBS), Grenoble, France;

[3] Univ. Grenoble Alpes, CNRS, CEA, EMBL Integrated Structural Biology Grenoble (ISBG), Grenoble, France;

[4] Institut de Chimie Moléculaire de l'Université de Bourgogne (ICMUB), CNRS UMR 6302, UBFC Dijon, 21078 Dijon, France;

[5] ARNA Laboratory, Université de Bordeaux, Inserm U1212, CNRS UMR 5320, IECB, Pessac 33607, France;

[6] UCIBIO, REQUIMTE, Departamento de Química, Faculdade de Ciências e Tecnologia, Universidade Nova de Lisboa, 2829-516, Caparica, Portugal;

[7] Associate Laboratory i4HB - Institute for Health and Bioeconomy, NOVA School of Science and Technology, NOVA University Lisbon, 2819-516 Caparica, Portugal;

* Corresponding author email: carlacruz@fcsaude.ubi.pt

Abstract

Let-7e precursor microRNA has the potential to adopt a G-quadruplex structure and recently, its key roles in oncology have been the focus of some studies, as it is now known that is frequently dysregulated in several cancer types. Therefore, it is crucial to unveil and fully characterize its capability to adopt a G-quadruplex structure and to be stabilized or destabilized by small molecules and proteins such as, nucleolin, a protein that is deeply associated with miRNA biogenesis. Herein, by combining a set of different methods such as circular dichroism, nuclear magnetic resonance, UV spectroscopy (thermal difference spectra and isothermal difference spectra), and polyacrylamide gel electrophoresis we demonstrate the formation and stabilization of the rG4 structure found in let-7e pre-miRNA sequence in the presence of K^+ (5'-GGGCUGAGGUAGGAGG-3'). The ability of eight small molecules to bind to and stabilize the rG4 structure was also fully assessed. The dissociation constants for each RNA G-quadruplex/small molecule complex, determined by surface plasmon resonance, ranged in the 10^{-6} to 10^{-9} M range. Lastly, the binding of the G-quadruplex structure to nucleolin in the presence and absence of each small molecule was evaluated via circular dichroism, surface plasmon resonance, polyacrylamide gel electrophoresis and confocal microscopy. The small molecules 360A and PDS demonstrated attractive properties to target and control the G-quadruplex structure of let-7e precursor microRNA. Furthermore, our findings highlighted that the interaction of TMPyP4 with the G-quadruplex of let-7e precursor miRNA could block the formation of the complex between the RNA G-quadruplex and nucleolin. Overall, this study introduces an approach to target the G-quadruplex found in let-7e pre-miRNA and opens up a new opportunity to control the microRNA biogenesis of let-7e miRNA.

Keywords: let-7e pre-miRNA; G-quadruplex; small molecules; nucleolin; interaction.

1. Introduction

RNA G-quadruplexes (rG4s) have been studied in the last few years due to intrinsic features that confer them, under certain circumstances, some advantages over their DNA counterparts [1,2]. Among these advantages, single-strand RNA lacks a complementary strand, which facilitates the intramolecular folding into secondary structures (including G4s) known to dictate their cellular functions [3]. Recently the structural complexity of rG4s has been discussed [4] but the vast majority of rG4s adopt a parallel topology, which simplifies the development of small molecules to target these structures [5].

To date, much attention has been paid to the study of G4s in precursor microRNAs (pre-miRNAs), suggesting a possible role of rG4s in the regulation of miRNA biogenesis [6]. Previous works have described the formation of G4s in pre-miRNA-149 [7], -92b [8], -26a [9], and -1229 [10], including our recent studies on rG4-forming sequences of pre-miRNA-149 (5'-GGGAGGGAGGGACGGG-3') [11] and -92b (5'-GGGCGGGCGGGAGGG-3') [12]. Furthermore, some studies explored and proved the formation of rG4 structures in miRNA-149 [13], -197 [13], -432 [13], -765 [13], -1587 [14] and -3620 [15]. The formation of the rG4 structure in let-7e pre-miRNA (rG4-let-7e) has also been reported [16] by Pandey *et. al*, who showed that rG4-let-7e could significantly influence miRNA biogenesis [16] notably *via* a Dicer cleavage assay. In fact, a recent study demonstrated that both DNA and RNA G4s could inhibit the cleavage of pre-miRNAs by Dicer [17]. However, a deeper biophysical characterization of the pre-miRNA G4s is of utmost importance to pave the way for developing new therapeutic approaches.

Let-7 family is deregulated in various cancers [18] but its exact function is not yet fully understood. Several lines of evidence have shown the key roles of let-7 in oncology, as it is now known that let-7e miRNA is frequently down-regulated in cancers. In addition, let-7e is associated with shorter overall survival of cancer patients [19,20], is implicated in the

modulation of drug sensitivity in certain cancers [21], and is one of the miRNAs that influenced γH2AX foci formation, a marker of double-strand break [22]. With this in mind, an appealing therapeutic strategy would be to control miRNA biogenesis *via* the use of small molecules (ligands) that could modulate the equilibrium between rG4 and stem−loop structures in pre-miRNAs [23–25]. However, this approach is, to date, underexplored since few rG4 structures have been characterized in terms of biological function and structure.

Another possible approach is to consider the protein partners of miRNA, chief among them is nucleolin (NCL), known to be deeply involved in miRNA biogenesis [26]. NCL is predominantly located in the nucleolus but, in a cancerous context, can be found in the cytoplasm and cell surface [27,28]. As it is established that NCL binds to and promotes the folding of G4 structures [29], its cytoplasmic location in cancer cells led to the possibility that NCL modulates the formation of G4 structures in pre-miRNAs.

Here, we sought out to investigate the rG4 biology and partners of a rG4-forming sequence found in let-7e pre-miRNA (5'-GGGCUGAGGUAGGAGG-3'). To this end, we first characterize the rG4 structure by circular dichroism (CD), UV absorption and nuclear magnetic resonance (NMR). Next, we study the interacting properties of 8 well-known G4 ligands by CD-melting, Fluorescence Resonance Energy Transfer (FRET)-melting and Surface Plasmon Resonance (SPR) measurements. Finally, we investigate the binding of NCL in the presence and absence of ligand by CD, SPR, polyacrylamide gel electrophoresis (PAGE) and confocal microscopy.

2. Materials and Methods

2.1. Oligonucleotides and ligands

Oligonucleotides were obtained from Eurogentec (Belgium) with HPLC-grade purification. rG4-let-7e oligonucleotides used in this work are 5'-GGGCUGAGGUAGGAGG-3', 5' biotin-GGGCUGAGGUAGGAGG-3', and 5′ -FAM GGGCUGAGGUAGGAGG TAMRA-3′ . The duplex sequence d(TATAGCTAT-hexaethyleneglycol-TATAGCTATA) labeled with FAM and TAMRA was also used. Stock solutions of approximately 1 mM were prepared using DEPC water (Sigma-Aldrich, USA) and stored at −80 °C until used. The concentration of oligonucleotide samples was determined from the absorbance at 260 nm by using the molar extinction coefficient. Annealing of oligonucleotide sequences was carried out by heating the samples for 10 min at 95 °C and cooling them on ice for 20 min before the experiments. Synthesis and purification of the ligand C_8 (10-(8-(4-iodobenzamide)octyl))-3,6-bis(dimethylamine) acridinium iodide) was performed as previously described [30]. The detailed synthesis and characterization of BioTASQ were performed as previously depicted [31]. The ligands PhenDC3 (3,3′ -[1,10-phenanthroline-2,9-diylbis(carbonylimino)]bis[1-methylquinolinium] 1,1,1-trifluoromethanesulfonate [32]; CAS: 929895-45-4), PDS (3-{1-[3-(dimethylamino)propyl]-2-methyl-1H-indol-3yl)-1H-pyrrole-2,5-dione [33]; CAS: 1085412-37-8), carboxyPDS 4-[[[2,6-Bis[[[4-(2-aminoethoxy)-2-quinolinyl]amino]carbonyl]-4-pyridinyl]oxy]methyl]-1H-1,2,3-triazole-1-propanoic [34]; CAS: 1417638-60-8), BRACO-19 (N,N′-(9-(4-(dimethylamino)phenylamino)acridine-3,6-diyl)bis(3-(pyrrolidin-1-yl)propanamide) [35]; CAS: 1177798-88-7), TMPyP4 (tetra-(N-methyl-4-pyridyl)porphyrin [36]; CAS: 36951-72-1) and 360A (2,6-N,N′-methyl-quinolinio-3-yl)-pyridine dicarboxamide) [37]; CAS: 794458-56-3) were obtained from Sigma-Aldrich (USA). The chemical structures of each ligand are depicted in **Figure 1**. Stock solutions of the compounds were prepared as 10

mM solutions in dimethyl sulfoxide (DMSO, Thermo Fisher Scientific, USA) and their subsequent dilution was done using nuclease-free water.

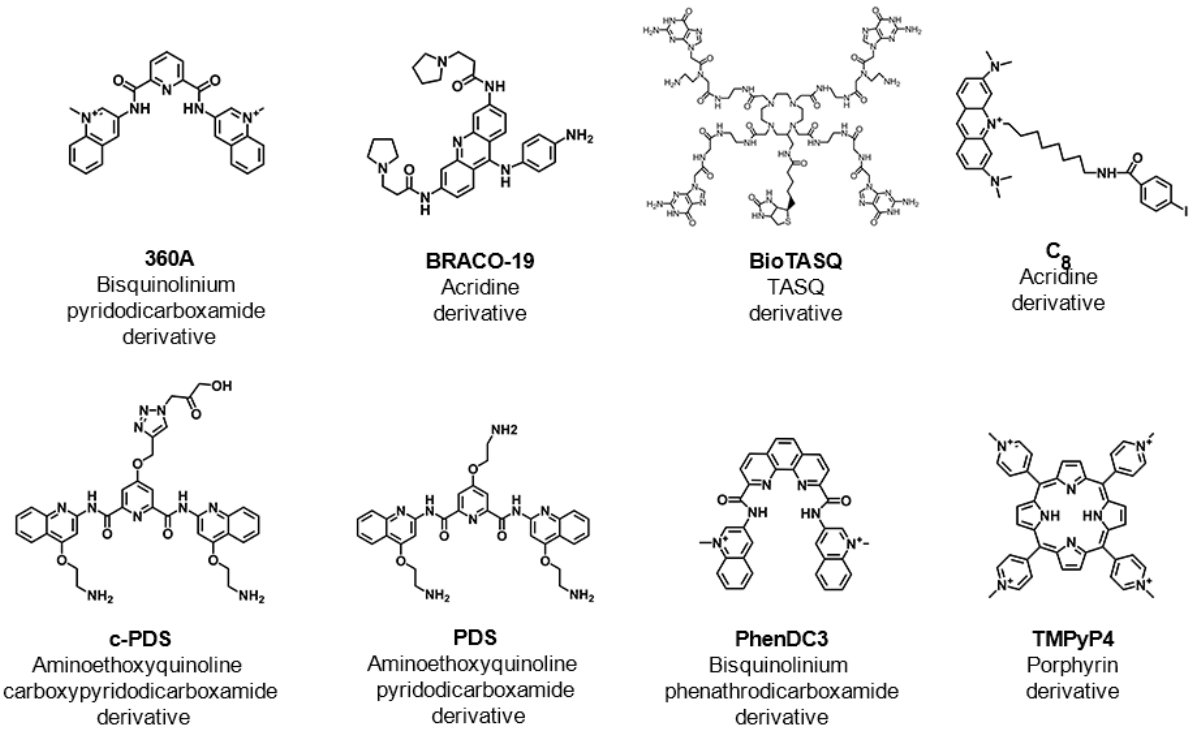

Figure 1. Chemical structure, common name and family of the ligands used in this work (chemical backbone).

2.2. Cloning, cell-free and purification of NCL RBD1,2

The sequence corresponding to NCL RNA binding domain (RBD) 1 and 2 was cloned into a pIVEX 2.4D vector. NCL RBD1,2 was synthesized *in vitro* using a cell-free expression system (ISBG, Grenoble). Briefly, NCL RBD1,2 was expressed under RNAse-free conditions in dialysis mode for 16 h at 23 °C under gentle agitation. The cell-free mixture contained 16 µg/mL of pIVEX 2.4D plasmid encoding the NCL RBD1,2 sequence, 1 mM of each essential amino acid, 0.8 mM of each rNTPs (guanosine-, uracil-, and cytidine-5'-triphosphate, 55 mM HEPES (pH 7.5), 68 µM folinic acid, 0.64 mM cyclic adenosine monophosphate, 3.4 mM dithiothreitol, 27.5 mM ammonium acetate, 2 mM spermidine, 80 mM creatine phosphate, 208 mM potassium glutamate, 16 mM magnesium acetate, 250 µg/mL creatine kinase, 27 µg/mL T7 RNA polymerase, 0.175 µg/mL tRNA, and 400 µL/mL S30 E. coli bacterial extract. After

incubation, the reaction mixture was diluted in binding buffer (50 mM HEPES (pH 7.5), 300 mM NaCl, and 10 mM imidazole) to a final volume of 45 mL and centrifuged for 45 min at 36,000 g at 4 °C. Thereafter, the supernatant was applied onto a 5 mL Ni-NTA column that had been previously equilibrated in binding buffer (50 mM Hepes (pH 7.5), 300 mM NaCl and 10 mM Imidazole) at 4 °C. The column was washed with 5 % of elution buffer (50 mM HEPES (pH 7.5), 300 mM NaCl, and 500 mM imidazole) to eliminate residual contaminants and the protein was eluted with 50 % of elution buffer. The fraction containing the NCL RBD1,2 was pooled and concentrated on a 10-kDa cut-off membrane. The purity of each fraction was analyzed by SDS-PAGE and the protein was identified through western blot analysis by using the primary anti-NCL antibody (Thermo Fisher, ref. PA3-16875).

2.3. UV Absorption spectroscopy

UV experiments were performed using a Thermo Scientific TM Evolution TM201 UV–Vis spectrophotometer (Thermo Fisher Scientific, Waltham, MA, USA) and recorded between 220–340 nm. Spectra acquisition was conducted with a 600 nm/min scanning rate, 1 nm data intervals, and 0.05 s of integration time. The rG4-let-7e sequence was diluted to 5 μM in lithium cacodylate buffer (10 mM, pH = 7.2). Thermal difference spectra (TDS) were carried out at 95 °C and 25 °C, corresponding to the unfolded and folded states, respectively. The TDS spectrum was calculated by subtracting the 25 °C spectra from the obtained at 95 °C. The difference spectrum was normalized relative to the maximum absorbance. The experiment was performed in 20 mM phosphate buffer pH 7.1 supplemented with 100 mM KCl. Isothermal difference spectra (IDS) were acquired at 25 °C and calculated by subtraction of the UV spectra of oligonucleotides, acquired in the absence or presence of increasing amounts of KCl.

2.4. Circular dichroism spectroscopy

CD spectra were acquired in a Jasco J-815 spectrometer (Jasco, USA), using a Peltier temperature controller (model CDF-426S/15). rG4-let-7e sequence was annealed as previously described. A 1 mm path-length quartz cuvette (Hellma, Germany) was used with rG4-let-7e at 10 µM in 10 mM lithium cacodylate buffer (Sigma-Aldrich, USA) at pH 7.2, supplemented with KCl (Thermo Fisher Scientific, USA). The required volume for the titrations was added directly to the quartz cell. The CD melting experiments were performed in the temperature range of 20-100 °C, with a heating rate of 2 °C/min by monitoring the ellipticity at 262 nm. Spectra acquisition was performed in the absence and presence of increasing concentrations of KCl or ligands. Data was converted into fraction folded (f) plots.

$$f = \frac{CD - CD_{\lambda}^{min}}{CD_{\lambda}^{max} - CD_{\lambda}^{min}} \quad (1)$$

where CD is the ellipticity of the monitored wavelength at each temperature and CD_{λ}^{min} and CD_{λ}^{max} are the lowest and highest ellipticity values, respectively. Data points were then fitted to a Boltzmann distribution equation (OriginPro 2016) and the melting temperatures were determined.

2.5. NMR spectroscopy

Standard zgesgp pulse sequence was used to acquire individual ^{1}H NMR spectra with water suppression using excitation sculpting, on a 600 MHz Bruker Avance III spectrometer equiped with a QCI cryoprobe. rG4-let-7e sequence was used at a concentration of 100 µM with a total volume of 200 µL in a 3 mm NMR tube, annealed as described above and supplemented with 10% D_2O (Eurisotop, France). The required volume for titrations was added directly to NMR tubes. The spectra of rG4-let-7e sequence in 20 mM phosphate buffer pH 7.1 supplemented with 100 mM KCl were acquired at different temperatures (17, 27, 37 and 47 °C). All the spectra

were acquired and processed with the software Topspin 3.1. Figures were prepared using TopSpin 4.0.6. Chemical shifts (δ) are reported in ppm.

2.6. Fluorescence Resonance Energy Transfer (FRET) Melting

FRET melting experiments were performed using a CFX Connect™ Real-Time PCR Detection System (Bio-Rad, Hercules, CA, USA), equipped with a FAM filter (λ_{ex} = 492 nm; λ_{em} = 516 nm). Oligonucleotides at 0.2 μM were annealed in lithium cacodylate (10 mM, pH 7.2) supplemented with 100 mM KCl before the experiment as described in the above sections. Each experimental condition was tested in duplicate in three separate plates. For each condition, 20 μL of oligonucleotides was aliquoted into each strip, followed by 5 μL of ligands solutions, at five different final concentrations (1, 2 and 5 eq.). Then, this was followed by an incubation time of 30 min at room temperature. The thermocycler was parametrized to measure and acquire the FAM emission after each step with a stepwise increase of 1 °C every 1 min, from 25 °C to 95 C. Through the fluorescence normalized curves, specifically to values when normalized emission is 0.5, the T_m values were ascertained for each type and concentration of ligand.

2.7. Surface Plasmon Resonance (SPR) Biosensor

SPR analysis was conducted on a Biacore T200 (Biacore, GE Healthcare, Uppsala, Sweden) with a SA sensor chip (streptavidin-coated sensor chip) (GE Healthcare, Sweden). The biotin-labeled rG4-let-7e (25 nM dissolved in 20 mM phosphate buffer supplemented with 100 mM KCl) was annealed as previously stated. The sensor chip was equilibrated with running buffer (20 mM phosphate buffer supplemented with 100 mM KCl) at 25 μL/min for 1 h. The flow cell was activated by injection of 1 M NaCl, 50 mM NaOH for 3 min. The injection was repeated seven times to remove unbound streptavidin from the sensor chip. Finally, to ensure surface stability, two primes with running buffer were performed and the buffer was flowed for 10 min

at 1 μL/min to obtain a stable baseline. The biotin-labeled rG4-let-7e (25 nM) was immobilized at 1 μL/min until it reached approximately 250 RU.

For kinetic/affinity analysis, each ligand was serially diluted in running buffer, ranging the concentration from 1 nM to 1 μM. All experiments were performed in triplicate at 25 °C. Each ligand was injected from low to high concentrations during 75 s with a flow rate of 50 μL/min, followed by dissociation of 600 s. Surface regeneration was achieved by injecting two pulses of 30 s of 10 mM glycine/HCl pH 1.5, and the next three 60 s injections of running buffer to remove any trace of regeneration solution.

BiaEvaluation Software was used for data analysis and the likelihood of fittings was assessed through the statistical parameters of Chi2 and U-value. All sensorgrams were double corrected for non-specific binding and refractive index changes (bulk effect) by subtracting the signals of an equivalent injection across the reference flow cell 1. Dissociation constants were obtained from the 1:1 affinity model of sensorgrams.

2.8. Non-denaturing polyacrylamide gel electrophoresis

Non-denaturing polyacrylamide gel (15%) electrophoresis was used to visualize the oligonucleotides. rG4-let-7e samples were prepared at a concentration of approximately 2 μM. Sucrose (Sigma-Aldrich, USA) was added to the samples at a final concentration of 23%. The oligonucleotide marker was loaded in parallel on the gel. The rG4-let-7e sequence was injected with and without KCl. A molar ratio of 1:1 of rG4-let-7e/ligand, rG4-let-7e/NCL RBD1,2 and rG4-let-7e/TBA was prepared, and the mixture was incubated for 30 min. The supramolecular complexes of rG4-let-7e/ligand/NCL RBD1,2 were prepared at a molar ratio of 1:1:1. The samples digested with RNase H (0.3-U/μL) (NZYtech, Portugal) were incubated for 3 h at 37 °C. Electrophoresis was performed at 120 V with a temperature close to 20°C. After

electrophoresis, the gel was stained by SYBR Gold (Invitrogen, USA) for 10 min under gentle agitation and visualized using ChemiDoc™ MP Imaging System (Bio-Rad, USA).

2.9. Confocal microscopy

A549 cell line was grown in Ham's F12 medium supplemented with 10% (v/v) FBS and 1% (v/v) penicillin-streptomycin. Cultures were maintained in a humidified chamber at 37 °C and 5% CO_2. The cells were subsequently seeded in μ-Slide 8-well flat bottom imaging plates (Ibidi GmbH, Germany) at a plating density of 5×10^4 cells/well and incubated for cell adhesion in humidified atmosphere at 37 °C and 5% CO_2. After 24h, cells were incubated for 2 h at 37 °C with primary anti-NCL antibody (PA3-16875, Invitrogen, USA; dilution of 1: 100). Following primary anti-NCL antibody incubation, cells were washed 3× with fresh serum-free medium and incubated with secondary antibody anti-rabbit IgG conjugated with Alexa Fluor® 647 (Thermo Scientific, USA; dilution of 1:500) for 1 h at 37 °C. Thereafter, cells were washed 3 × with fresh serum-free medium and incubated with rG4-let-7e labelled at the 5' terminus with Cyanine-3.5 (Cy3.5) (1 μM) for 1 h. Then, cells were washed 3 × with fresh serum-free medium and stained with Hoechst 33342® nuclear probe (Thermo Scientific, USA; 2 μM) for 15 min. Then, cells were imaged using a Zeiss LSM 710 confocal laser scanning microscope (Carl Zeiss, Germany) and processed using the blue edition of ZEN 2012 software (Carl Zeiss, Germany).

3. Results

3.1. Putative rG4 sequence in let-7e pre-miRNA adopt a G4 structure in presence of K^+

To support the formation of the rG4-let-7e, we carried out standard spectroscopic assays such as UV isothermal difference spectra (IDS), UV thermal difference spectra (TDS), CD and NMR of the short 16-nt-long G-rich sequence (5'-GGGCUGAGGUAGGAGG-3').

Using IDS, we found the cation-dependent nature of the rG4-let-7e. The IDS spectra showed negative peaks around 295 nm and positive peaks around 275 nm in the presence of KCl concentration above 10 mM, which indicated the formation of a rG4 structure (**Figure 2A**). Next, TDS signatures were recorded on rG4-let-7e in the presence of 100 mM KCl, by subtracting the absorbance spectrum at 25 °C (rG4 is fully folded) from the absorbance spectrum at 95 °C (rG4 is fully unfolded). In line with IDS, a prominent negative peak at 295 nm and a positive peak at 275 nm were observed (**Figure 2B**), indicative of the rG4 formation [38]. The intense negative peak suggests that the rG4-let-7e sequence had a higher propensity to form a rG4 structure.

CD measurements were also performed to confirm the rG4 signature and evaluate the effect of KCl. Results seen in **Figure 2C** showed an increase in the ellipticity upon addition of 100 mM KCl, with a CD signature typical of a parallel G4 (positive band ~ 260 nm and a negative band ~ 240 nm). In order to evaluate the influence of KCl in the thermal stabilization of the rG4 structure, CD-melting experiments were performed in the absence or presence of 100 mM KCl: without KCl, the mid-transition temperature was 39.9 ± 0.4 °C, while the presence of 100 mM KCl increased it to 51.1 ± 0.2 °C (**Figure 2D**). Altogether, these biophysical results confirm that rG4-let-7e sequence folds into a stable rG4 structure in presence of 100 mM KCl.

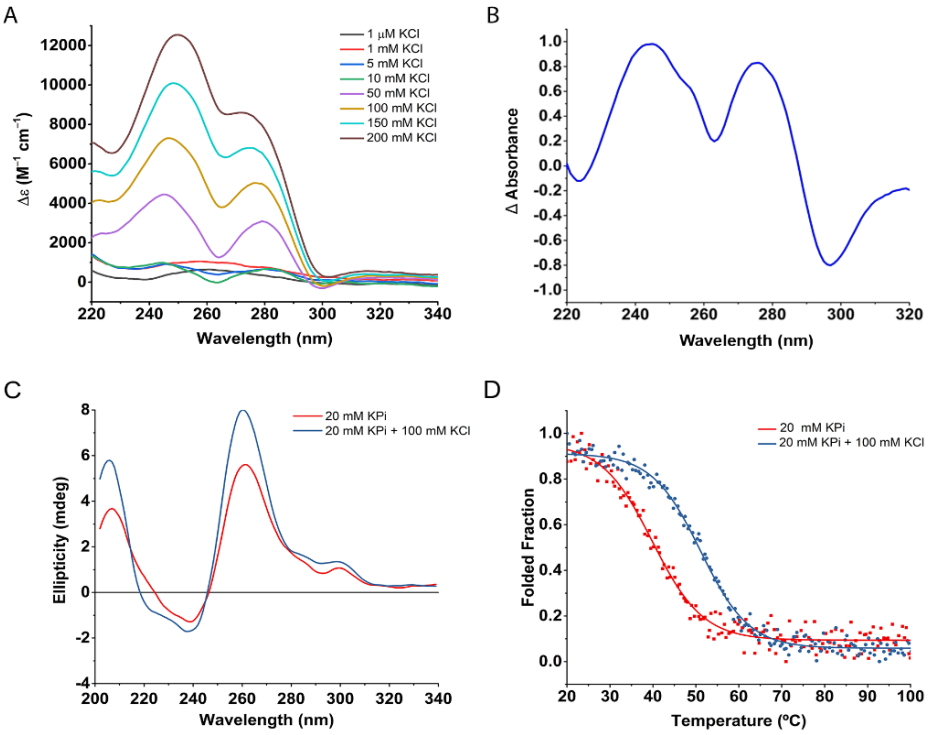

Figure 2. (A) IDS steady state of rG4-let-7e in the presence of increasing amounts of KCl. **(B)** TDS spectrum in the presence of 20 mM phosphate buffer, pH 7.1 supplemented with 100 mM KCl **(C)** CD spectra of the putative rG4, found in let-7e pre-miRNA, at 10 µM in 20 mM phosphate buffer, pH 7.1 in the absence and presence of 100 mM KCl. **(D)** CD-melting curves of the putative rG4-let-7e at 10 µM in 20 mM phosphate buffer, pH 7.1 in the absence and presence of 100 mM KCl.

To better characterize the structure of rG4-let-7e, ^{1}H NMR spectroscopy was employed. rG4 structures present a set of imino protons in the 10-12 ppm range, characteristic of Hoogsteen base pairs [39]. The experiments were performed in the absence and presence of increasing concentrations of K^{+} and the results seen in **Figure 3** revealed that at low K^{+} concentrations (< 5 mM KCl), the sequence does not fold into a rG4 structure. However, the imino protons are easily observable at 10 mM of KCl but are not well-resolved, while a distinct set of 8 imino proton signals can be observed in concentrations of KCl >50 mM, indicating a single G4 structure with two G-tetrads. The imino proton pattern does not change significantly between 50 and 100 mM KCl, which suggests that the rG4 structure is fully folded in the presence of 50 mM KCl. Variable temperature ^{1}H NMR experiments (**Figure S1**) confirmed

the stability of rG4-let-7e since the structure is maintained up to 47°C. These results are thus fully in line with those obtained by IDS and TDS experiments.

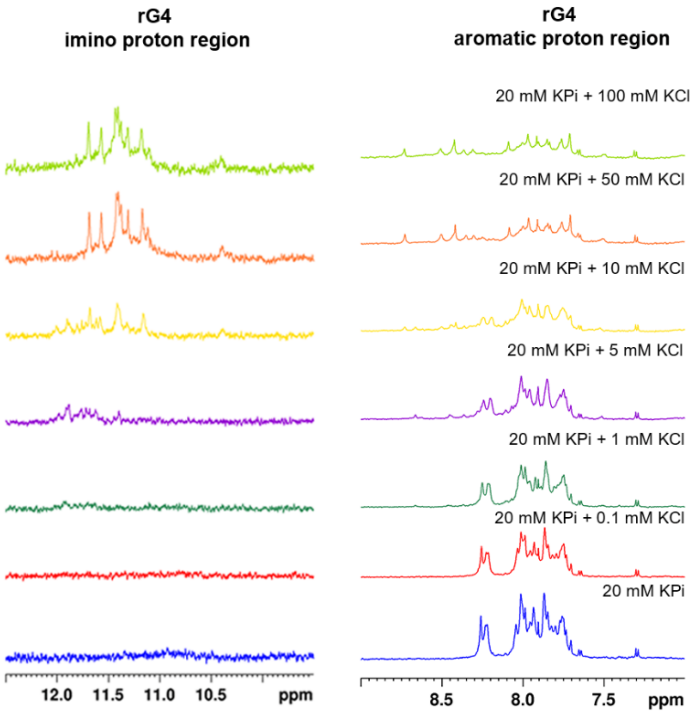

Figure 3. ^{1}H NMR spectra of the imino and aromatic proton region of the putative rG4-let-7e (100 µM) in Phosphate buffer containing 20 mM K_2HPO_4/KH_2PO_4, and different concentrations of KCl in the range 0-100 mM. All the ^{1}H NMR spectra were acquired at 27 °C.

3.2. Stabilization of rG4-let-7e by G4 ligands

Next, we investigated the interaction of well-known G4 ligands with the rG4-let-7e, *via* Fluorescence Resonance Energy Transfer (FRET)-melting experiments performed with TAMRA/FAM-labelled rG4-let-7e and a selection of ligands very heterogeneous in nature (**Figure 1**). The experiments were carried out at different ligand concentrations. The results seen in **Figure 4A** and **Table S1** revealed that melting temperature of the rG4 in the presence of 100 mM KCl was 57.3 °C. The highest stabilzations were obtained with 360A, PDS and TMPyP4, with ΔT_m = 24, 15.8 and 22.7 °C at 5 mol. eq., respectively. As further discussed, hereafter, TMPyP4 has an ambivalent impact on G4 stabilization, depending on whether it is

used at 1, 2 or 5 mol. equiv.; this is also the case for C_8, which displays a slight destabilizing effect at 2 mol. eq. but a small stabilizing effect at 5 mol. eq. Both established rG4 ligands, BioTASQ and carboxy-PDS (c-PDS) failed to stabilize rG4-let-7e in our conditions, which is not surprising for the former as the biotin appendage is known to 'poison' one of the G arms when free (that is, when not embedded in a biotin/streptavidin complex) [40].

CD spectroscopy was then implemented with each rG4/ligand pair (seen in **Figure S2**) and showed a distinct ellipticity behavior: at 2 mol. eq. concentration, 360A, BioTASQ, C_8 and PhenDC3 do not affect CD signature, while a higher concentration led to a slight increase in ellipticity; conversely, at 2 mol. eq. concentration, BRACO-19, c-PDS, PDS and TMPyP4, the ellipticity decreases, while keeping the overall rG4 topology. These observations are in line with previous results notably for BRACO-19, whose quite surprising G4-destabilizing properties (at low concentration) was confirmed through a series of *in vitro* techniques, and for TMPyP4, which triggers both partial rG4 unfolding (at low concentration), stabilization and then, rG4 aggregation at higher concetrations [41–43].

CD-melting was also performed and collected results (**Figure 4B, Figure S3 and Table S3**) confirmed a strong stabilizing effect for 360A, PDS, PhenDC3 and TMPyP4, with $\Delta T_m >$ 20 °C. The other ligands (BRACO-19, BioTASQ, C_8 and c-PDS) showed only weak stabilizing effects. Overall, these results are in line with those obtained by FRET-melting experiments, with the notable exception of PhenDC3, found to be a modest rG4 binder by FRET-melting assay and an excellent one in CD-melting experiments.

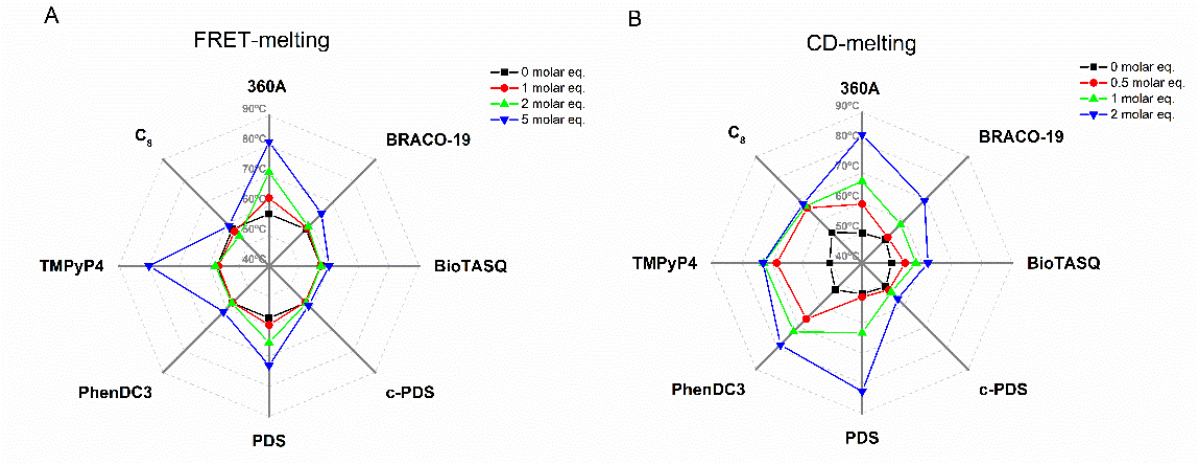

Figure 4. T_m radar plots of rG4-let-7e in the presence of different molar equivalents of G4 ligands, obtained by **(A)** FRET-melting and **(B)** CD-melting experiments.

3.3 Binding affinity of G4 ligands towards rG4-let-7e

We further quantified the binding affinities of these ligands by SPR. The dissociation constant (K_D) was determined using a biotin-labeled rG4-let-7e sequence immobilized on the surface of streptavidin sensor chips. The SPR signal responses related to the specific interaction with the rG4-let-7e were obtained after subtraction of the signals recorded on the reference flow-cell and the running buffer injection by applying a double referencing procedure. The K_D was obtained by fitting the steady-state response vs. the ligand concentration by Langmuir isotherm according to a 1:1 binding stoichiometry (**Figure S4**). The obtained K_D values, seen in **Table 1**, revealed that all ligands bind to rG4-let-7e with high affinity. These results do not fully agree with melting-based results, notably for C_8 and c-PDS, found to be modest thermal stabilizers but to display high binding affinity by SPR ($K_D = 3.09 \times 10^{-9}$ and 6.43×10^{-8} for C_8 and c-PDS, respectively). On the opposite, 360A and PDS, which were found good thermal stabilizers provide low K_D values (6.56×10^{-6} and 3.81×10^{-6} M, respectively). These results highlight that a great caution must be exercised when dealing with *in vitro* investigations to determine the binding behavior of ligands as results can be found strongly dependent on the

technique implemented, thereby emphasizing the need to use and compare results collected with assays relying on different biophysical features.

Table 1. K_D constant values of rG4-let-7e in presence of G4 ligands measured by SPR biosensor.

Ligand	$K_D \pm$ SE (M)
360A	$6.56 \times 10^{-6} \pm 1.1 \times 10^{-6}$
BioTASQ	$1.17 \times 10^{-6} \pm 2.6 \times 10^{-7}$
BRACO-19	$2.68 \times 10^{-7} \pm 7.3 \times 10^{-8}$
C_8	$3.09 \times 10^{-9} \pm 1.1 \times 10^{-9}$
c-PDS	$6.43 \times 10^{-8} \pm 1.6 \times 10^{-8}$
PDS	$3.81 \times 10^{-6} \pm 1.3 \times 10^{-6}$
PhenDC3	$5.37 \times 10^{-8} \pm 1.8 \times 10^{-8}$
TMPyP4	$2.49 \times 10^{-7} \pm 2.9 \times 10^{-8}$

3.4. Molecularity and structural nuances of rG4-let-7e in the presence of G4 ligands

The molecularity of the rG4-let-7e and rG4-let-7e/NCL RBD 1,2 complexes was evaluated by polyacrylamide gel electrophoresis (PAGE). The oligonucleotides were diluted to 2 μM and complexes with ligands and/or NCL RBD 1,2 were prepared at a 1:1 molar ratio. The electrophoretic profiles seen in **Figure S5** indicated that rG4-let-7e displays a major conformation in both K^+-free and K^+-rich conditions but in water the electrophoretic profile showed a smear along the run and two bands with less intensity at molecular weight around 60 nt. In the presence of BioTASQ, BRACO-19, C_8, c-PDS, PDS and PhenDC3, the electrophoretic bands retained the same intensity of that observed in K^+-rich conditions and, while TMPyP4 trigger band smear, in line with their aggregation properties (as previously described [42]). c-PDS depicted the same major conformation with the same intensity, but a small smear was observed at high molecular weight (above 90 nt.), suggesting the formation of

a molecular specie not structurally defined enough to yield to an isolated, well-defined band. Of note, 360A association results in a band with less intensity and low molecular weight, indicating a stronger association.

These results prompted us to investigate further the interactions of rG4-let-7e with 360A, PDS and TMPyP4 by ^{1}H NMR. Titrations performed with 360A (**Figure 5A**) resulted in a broadening of the imino protons, suggesting a good but not well-defined binding of the ligand to the G4 structure [44]. PDS elicited the same behavior (**Figure 5B**), while the imino proton signals of the rG4 totally disappeared in the presence of 0.5 molar eq. of TMPyP4 (**Figure 5C**), which again advocates for a ligand-induced aggregation.

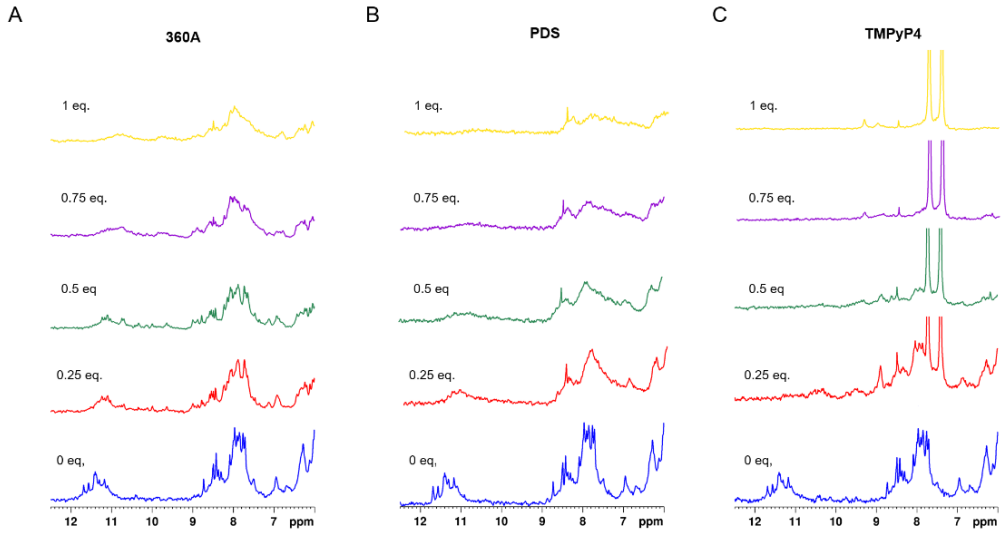

Figure 5. ^{1}H NMR spectra of the imino and aromatic proton region of the rG4-let-7e (100 µM) upon titration with **(A)** 360A, **(B)** PDS and **(C)** TMPyP4. Spectra were acquired in phosphate buffer containing 20 mM K_2HPO_4/KH_2PO_4 at 27 °C.

In silico studies (molecular docking and molecular dynamics simulations) can provide in some cases insights into the rG4 binding mode of ligands at the molecular level. Since the solution structure of rG4-let-7e is not available, we first used the 3D-NuS algorithm for generating the rG4-let-7e 3D structure [45]. The model was re-optimized by running fully

solvated MD simulation during 20 ns. The representative model of the MD simulation is shown in **Figure S6**: in this model, the rG4 is made of two stacked G-tetrads (G1-G8-G12-G15 and G2-G9-G13-G16) interconnected by one long, 5-nt loop (GCUGA) and two short loops (UA and A). The residues belonging to the long loop appear to point inward, while that of the short loops outward. The long loop can facilitate the binding of the ligands (as recently demonstrated for porphyrinic ligands) [46], while end-stacking interactions can be observed since no end-capping residues are present. The binding mode of each ligand to the 3D structure of rG4-let-7e was also investigated by molecular docking and molecular dynamics (**Figures S7-S8**); however, the results were not conclusive.

3.5. Binding of NCL RBD1,2 to rG4-let-7e structure

We thoroughly described (above) the interactions that take place between rG4-let-7e and a selected panel of ligands; it was thus of interest to investigate the interactions of both rG4 and rG4/ligand complexes with the NCL RBD 1,2 *via* CD, SPR and PAGE experiments.

CD measurements were carried out to assess the influence of the protein on the overall rG4-let-7el topology. Spectra seen in **Figure 6A** revealed a slight decrease of the ellipticity of the maximum positive band of the rG4 (264 nm), suggesting an interaction of the protein with the rG4 structure, and a strong increase of the negative bands, as a result of the contribution of the secondary structure of the NCL (the CD signature of NCL RBD1,2 displays a double negative band at around 210 and 220 nm) [47]. The thermal stability of the rG4-let-7e was evaluated by CD-melting experiments and showed a slight increase of the rG4 melting temperature in the presence of 10 μM NCL RBD1,2 (ΔT_m = 2.9 °C, **Figure 6B**), indicating a weak but detectable interaction of rG4-let-7e with NCL RBD1,2. This interaction was further characterized by SPR: the equilibrium binding affinity curve (**Figure 6C**) revealed that the K_D of the association of

NCL RBD1,2 with rG4-let-7e was in the micromolar range $1.91 \times 10^{-6} \pm 3.6 \times 10^{-7}$ M, again indicating a weak but reliably detectable interaction.

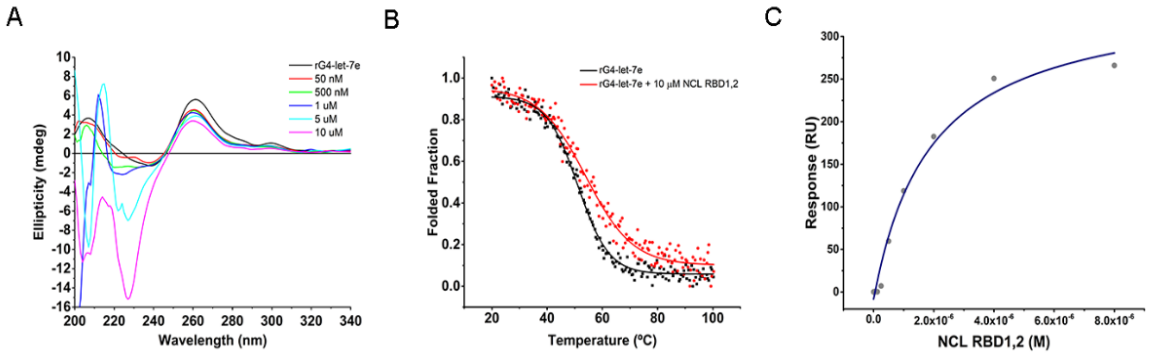

Figure 6. Molecular interaction of rG4-let-7e with NCL RBD1,2. **(A)** CD spectra of rG4-let-7e in the absence and presence of increasing amounts of NCL RBD1,2 (0-10 µM). **(B)** CD-melting curves of rG4-let-7e in the absence and presence of NCL RBD1,2. **(C)** Equilibrium binding curve of rG4-let-7e upon addition of increasing concentrations of NCL RBD1,2.

PAGE experiments were performed to evaluate the formation of the rG4-let-7/NCL RBD1,2 complex and the possible ternary rG4-let-7e/ligand/NCL RBD1,2 complexes. Results seen in **Figure 7A-B** showed a clear, concentration-dependent formation of the rG4/protein complex, illustrated by the increase of band intensity above 90 nt. Moreover, in the presence of 32 µM NCL RBD1,2, the band corresponding to rG4-let-7e almost disappeared, indicating the association of the rG4 structure with NCL RBD1,2. The presence of all ligands does not modify this electrophoretic profile, suggesting the possible formation of the ternary complex, with the notable exception of TMPyP4, which triggers the complete disappearance of the electrophoretic bands corresponding to the complex with NCL RBD1,2, again in line with a possible aggregation (**Figure 7C**). Since NCL was described to preferentially bind parallel G4 topologies, we also tested its ability to bind to a two G-tetrad antiparallel G4 topology, namely that adopted by thrombin-binding aptamer (TBA). The results seen in **Figure S9** revealed that in the presence of 32 µM NCL RBD1,2, the band corresponding to free TBA remains visible proving the less prominent binding of the antiparallel G4 topology to NCL RBD1,2.

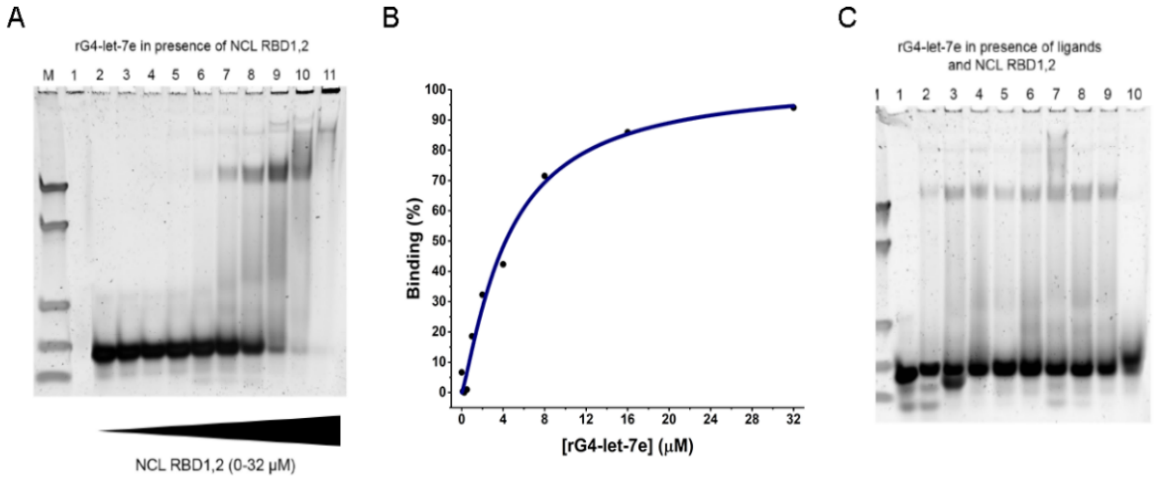

Figure 7. (A) Non-denaturing gel electrophoresis of rG4-let-7e (2 µM) in presence of different concentrations of NCL RBD1,2 (Lanes: M – Marker; 1 – NCL RBD1,2 (2 µM) ; 2 – rG4-let-7e without NCL RBD1,2; 3 – 0.1 µM; 4 - 0.250 µM; 5 – 0.5 µM; 6 – 1 µM; 7 - 2 µM; 8 – 4 µM: 9 – 8 µM; 10 – 16 µM and 11 – 32 µM). **(B)** Relative proportions of NCL RBD1,2-bound rG4-let-7e to unbound rG4-let-7e were quantified and plotted. **(C)** Non-denaturing gel electrophoresis of rG4-let-7e (2 µM) / ligand (2 µM) / NCL RBD1,2 (2 µM). (Lanes: Lanes: M – Marker; 1 – rG4-let-7e in 20 mM Phosphate buffer supplemented with 100 mM KCl; 2 – rG4-let-7e (2 µM) / NCL RBD1,2 (2 µM); 3 – 10 – ligands (2 µM) (3 - 360A; 4 – BioTASQ; 5 – BRACO-19; 6 – C_8 and 7 – c-PDS; 8 – PDS; 9 - PhenDC3; 10 - TMPyP4)).

3.6. Retention of rG4 structure in presence of ligands and ligands/NCL RBD1,2

To go a step further, we decided to digest rG4 samples with RNAse H, in absence and presence of K^+, ligands and/or both ligands and NCL RBD1,2. The PAGE experiments seen in **Figure 7A** were used as controls for these experiments: as seen in **Figure 8A**, the RNase H digestion was partial only in our conditions, since it resulted in a decrease of the intensity of the bands when compared with the control. The presence of K^+ favoured a fully folded and stable rG4, while that of ligands resulted in different situations: results obtained with BioTASQ, BRACO-19, C_8, c-PDS and PDS are comparable to that obtained without RNase H incubation, suggesting that these ligands do not affect the rG4 structure; PhenDC3 and TMPyP4 displayed less intense bands, suggesting an aggregation or an increased sensitivity to RNase H, which

could be rationalized for TMPyP4 (owing to its possible G4 destabilizing properties) but not for PhenDC3, thus supporting an aggregation. Only 360A provided a distinct signature, highlighting again its unique G4-interacting properties. We repeated these experiments in the presence of NCL RBD1,2 (**Figure 8B**): the rG4/NCL RBD1,2 was found to withstand digestion and, as above, the presence of BioTASQ, BRACO-19, C_8, c-PDS and PDS does not modify the electrophoretic profiles; however, noticeable differences were obtained with 360A, PhenDC3 and TMPyP4: the intensity of the corresponding bands strongly decreased and only the band corresponding to low molecular weight complexes were visible with 360A and TMPyP4, suggesting that these three ligands, 360A, PhenDC3 and TMPyP4, avoid the formation–or favour the disassembly–of the complex they formed with rG4 and NCL RBD1,2, and thus help RNase H processivity (to be compared with **Figure 7B**). These results thus offer a new perspective on the possible use of G4-targteing ligands to modulate miRNA biology.

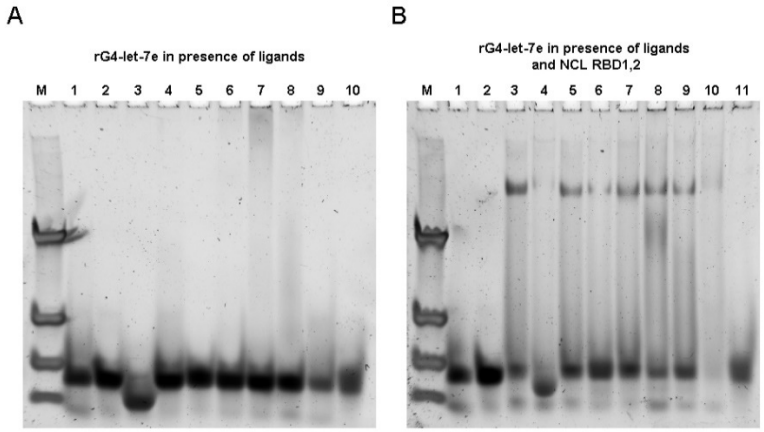

Figure 8. **(A)** Non-denaturing gel electrophoresis of rG4-let-7e (2 µM) without or with ligand (2 µM) in presence of RNase H (0.3 U/µL). (Lanes: M – Marker; 1 – rG4-let-7e in water; 2 – rG4-let-7e in 20 mM Phosphate buffer supplemented with 100 mM KCl; 3 – 10 – ligands (2 µM) (3 - 360A; 4 – BioTASQ; 5 – BRACO-19; 6 – C8 and 7 – c-PDS; 8 – PDS; 9 - PhenDC3; 10 - TMPyP4)). **(B)** Non-denaturing gel electrophoresis of rG4-let-7e (2 µM) / ligand (2 µM) / NCL RBD1,2 (2 µM) in presence of RNase H (0.3 U/µL). (Lanes: Lanes: M – Marker; 1 – rG4-let-7e in water; 2 – rG4-let-7e in 20 mM Phosphate buffer supplemented with 100 mM KCl; 3 – rG4-let-7e (2 µM) / NCL RBD1,2 (2 µM); 4 – 10 – ligands (2 µM) (4 - 360A; 5 – BioTASQ; 6 – BRACO-19; 7 – C8 and 8 – c-PDS; 9 – PDS; 10 - PhenDC3; 11 - TMPyP4)).

3.7. Targeting of cell surface NCL by rG4-let-7e and their complexes with ligands

Finally, we investigated the binding of rG4-let-7e to NCL in a cellular context *via* confocal laser scanning microscopy (CLSM), using the non-small cell lung cancer (NSCLC) cell line A549, known to overexpress NCL at the cell surface. Cells were incubated with rG4-let-7e labelled with Cy3.5 to monitor its cellular distribution. CLSM images seen in **Figure 9** confirmed the presence of NCL at the cell surface of NSCLC cells (arrows); upon incubation with rG4-let-7e/PDS (**Figure 9B**) and rG4-let-7e/TMPyP4 complexes (**Figure S10**), this colocalization can be modulated by the ligand, as PDS triggers an accumulation of common *foci*, in line with its G4-stabilizing properties, while TMPyP4 decreases them, again in line with their disrupting properties.

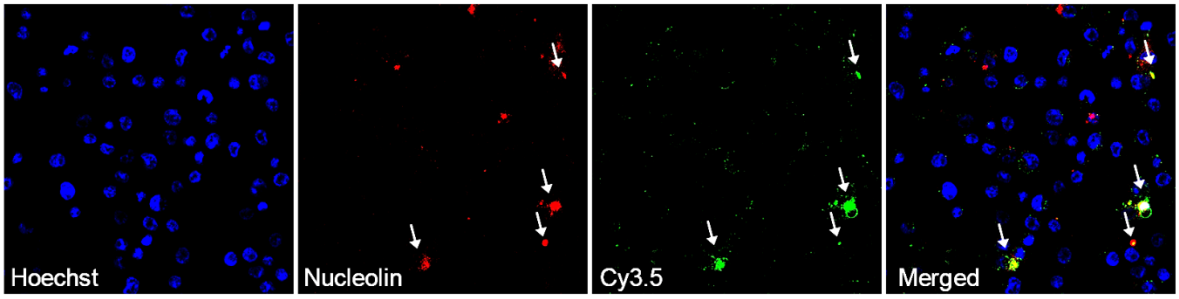

Figure 9. Confocal microscopy of A549 cells incubated with rG4-let-7e. For each panel, images showed the cells stained with Hoechst 33342® nuclear probe (2 µM, blue); rG4-let-7e Cy3.5 complex (1 µM, green); and NCL (red). NCL was labeled with the primary anti-NCL polyclonal antibody (1:100) and detected with the secondary antibody against IgG conjugated with Alexa Fluor® 647 (1:500). Arrows showed co-localization of rG4-let-7e and NCL.

4. Discussion

Among all tumor suppressor microRNAs, depletion of miR-let-7e expression frequently occurs in cancers and is strongly correlated with poor overall survival rates in cancer patients [48]. The short 16-nt-long G-rich sequence (5'-GGGCUGAGGUAGGAGG-3') found in let-7e pri- and pre-miRNA is a possible rG4-forming sequence that partially overlaps with let-7e-5p

sequence [16,49]. This was demonstrated by Pandey *et. al* who first demonstrated the formation of a rG4 structure in let-7e pre-miRNA in physiological conditions [16]. They notably transfected MCF-7 cells using both the rG4-forming wild-type let-7e pre-miRNA sequence and the mutant pre-let7e, for which the rG4 formation is precluded: their qRT-PCR analyses revealed a remarkable difference in mature miRNA levels, with a 5-fold decrease of mature let-7e in cells transfected with wild-type let-7e pre-miRNA. These results suggested an inhibitory effect of the rG4 structure in dicer activity. They also evaluated the impact of the ligand TMPyP4 on rG4 and indicated that the ligand might disrupt the rG4 structure. This effort was recently continued by Pandolfini *et al*. who explored the connection between the rG4 formation in let-7e pre-miRNA and G methylation (7-methylguanosine, m7G) [49]. They demonstrated that the methylation of G11 negatively impacted rG4 formation, likely affecting the structural equilibrium towards the stem-loop conformation. These results prompted us to further investigate the folding and stability of this rG4 structure and its interaction with well-known G4 ligands.

To this end, we applied a set of biophysical methods routinely used to characterize rG4 folding. Collectively, the results of CD, IDS and TDS experiments confirmed the formation of a parallel rG4 structure, found to be strongly dependent on K^+ concentration. Furthermore, in line with recent evidence on the unexpected structural complexity of rG4 structures, [4] we found an intriguing CD signature for rG4-let-7e, with a slight positive band around 295 nm: on the basis of what was described for the G4 structure found in *c-KIT* gene [50], notably its ability to form a parallel G4 containing an external loop, [50,51] we can postulate that rG4-let-7e might also have such a loop [52]. The structure of this rG4 was further characterized by ^{1}H NMR spectroscopy, which evidenced the formation of a two-quartet G4 core with 8 characteristic of Hoogsteen hydrogen bonds in the 10-12 ppm region [39] for KCl concentration higher than 5 mM.

Next, the ability of eight well-known G4-ligands to form a rG4-let-7e/ligand complex was investigated by CD- and FRET-melting experiments. Both pyridodicarboxamide (PDC)-based ligands, 360A and PDS, strongly stabilize rG4-let-7e, in line with results described by Kwok *et al*. who already describe the stabilization of the rG4 found in pre-miRNA-149 by PDS [7]. In sharp contrast, the behavior of TMPyP4 is dual, thermally stabilizing rG4-let-7e (CD- and FRET-melting) while triggering disruption and/or aggregation of rG4-let-7e in isothermal experiments (CD and PAGE). Again, these results fully comply with investigations recently performed by some of us, which describes the dual behavior of TMPyP4 as a function of its concentration (disrupting G4 at low concentrations while triggering aggregation at high concentrations) [42]. The properties of PhenDC3 were more puzzling, as it poorly stabilized rG4 (ΔT_m = 4.2 °C at 5 molar eq.) in FRET-melting experiments and strongly stabilized it (ΔT_m = 26 °C) in CD-melting experiments. This considerable difference is likely due to the use of fluorophores in FRET-melting experiments, which could lead to unspecific interactions of aromatic ligands [1,53]. The remaining ligands (BioTASQ, BRACO-19, C_8 and c-PDS) were found to be modest stabilizers in comparison. Again, the case of C_8 is unexpected since it has already been described as a strong stabilizer of the rG4s found in pre-miRNA-149 [11] and pre-miRNA-92b [12]. This difference can be ascribed to the structural features of these rG4s, pre-miRNA-149 and pre-miRNA-92b forming 3-tetrad rG4s with short loops (1-2 nt) while rG4-let-7e is a 2-tetrad rG4 with a long external loop (5 nt).

One of the conspicuous aspects of the present study is the variations of results between different *in vitro* techniques. Two illustrative examples are C_8 and c-PDS, with moderate stabilizing properties but excellent SPR results (with K_D values in the nanomolar range, 3.09×10^{-9} and 6.43×10^{-8}, respectively). On the other hand, 360A and PDS, which display high stabilizing properties, elicit K_D values in the micromolar range only (6.56×10^{-6} and 3.81×10^{-6} M, respectively). This brightly illustrates the need to implement different and complementary

biophysical techniques when searching for new ligands, to discard false positives and negatives in the most reliable fashion possible. Along this line, PAGE is an interesting assay as it uniquely allows for a direct analysis of the molecularity of nucleic acid structures [54]. The results obtained with rG4-let-7e in the presence of ligands revealed a strong association of 360A and confirmed the ability of TMPyP4 to aggregate rG4 (these results were corroborated by ^{1}H NMR titrations), while the results collected with the other ligands were less conclusive.

The biological activity of nucleic acids is mediated by their protein partners. We focused here on NCL, which is directly involved in several steps of miRNA biogenesis and is found to be involved in their aberrant processing linked with many cancers [55]. It is known that NCL can play a chaperone role in assembling G4 structures and binds more tightly to parallel topology [29,56]. We verified this investigating the binding of NCL to the antiparallel G4 TBA *via* a series of PAGE experiments which confirmed the tighter binding of NCL to rG4-let-7e as compared to TBA, with an affinity constant in the micromolar range ($1.91 \times 10^{-6} \pm 3.6 \times 10^{-7}$ M). These results corroborated CD, IDS and TDS experiments, which indicated a parallel G4 topology of rG4-let-7e in the presence of K^+. PAGE experiments also revealed the formation of the complex rG4-let-7e/NCL RBD1,2 and rG4-let-7e/ligand/NCL RBD1,2 for most if not all the ligands, with the notable exception of TMPyP4, which aggregates the rG4/NCL RBD1,2 complex.

The formation and stability of the rG4-let-7e structure in the cellular context are fundamental aspects of its functions in miRNA biogenesis. To assess this, we conducted an RNase H assay with the rG4 structure in the presence of K^+, ligands and NCL. This assay confirmed the proper folding, and thus, its stability, of the rG4-let-7e structure in a biologically relevant context (where K^+ is present in a concentration around 140–150 mM) [57,58]; next, it showed the ability of PhenDC3 and TMPyP4 to make the rG4 motif more sensitive to enzymatic digestion, on the basis of either G4 disruption or a possible aggregation/precipitation in the

condition of the assay [42]. With the notable exception of 360A, the other ligands poorly affect RNase H activity, even in the presence of NCL RBD1,2.

Finally, we demonstrated by CLSM the binding of rG4-let-7e to NCL present at the surface of A549 cells using a fluorescently labelled rG4-let-7e. These images revealed co-localization spots of rG4-let-7e and NCL, which can be modulated by ligands, with PDS that favors this association and TMPyP4 that precludes it, on the basis of our previous investigations in which cell surface NCL was targeted by the rG4 found in pre-miRNA-149 in the presence of the ligand C_8 [11].

Altogether, these results demonstrated the binding of the rG4 structure to ligands, NCL and ligand/NCL complex both *in vitro* and in cells, which supports the hypothesis according to which the biogenesis of let-7e miRNA could be modulated by targeting its rG4 structure with small molecules.

5. Conclusions

In summary, we have used biophysical methods to unravel the structure of rG4-let-7e. The biological relevance of let-7e is widely recognized and is linked to several hallmarks of cancer. We demonstrate here that the 16-nt sequence found in let-7e pre-miRNA (5'-GGGCUGAGGUAGGAGG-3') folds into a rG4 structure with two G-tetrads. The ability of 8 well-known ligands to interact with the rG4-let-7e structure, assessed by CD- and FRET-melting experiments, highlighted the enticing properties of 360A and PDS, while highlighting again the intricate nucleic acid-interacting properties of PhenDC3 and TMPyP4. We also investigate here the effect of NCL RBD1,2 in absence and presence of the ligands, demonstrating the possible existence of a ternary G4/ligand/protein. Altogether these results contribute to decipher the complex biology of miRNA and could pave the way towards the

control of miRNA biogenesis by targeting rG4 structures in pre-miRNAs by ligands and protein surrogates.

Conflicts of interest

There are no conflicts of interest to declare.

Acknowledgements

This work was supported by PESSOA program ref. 5079 and project "Projeto de Investigação Exploratória" ref. IF/00959/2015 entitled "NCL targeting by G-quadruplex aptamers for cervical cancer therapy" financed by Fundo Social Europeu e Programa Operacional Potencial Humano. This work benefited from access to the Cell-Free platform of the Grenoble Instruct-ERIC center (ISBG; UMS 3518 CNRS-CEA-UGA-EMBL), an Instruct-ERIC centre, within the Grenoble Partnership for Structural Biology (PSB), supported by FRISBI (ANR-10-INBS-0005-02) and GRAL, financed within the University Grenoble Alpes graduate school (Ecoles Universitaires de Recherche) CBH-EUR-GS (ANR-17-EURE-0003). Financial support was provided by Instruct-ERIC (PID: 10168 "Production of the full-length nucleolin for structural studies"). Thanks are due to FCT/MCT for the financial support to CICS-UBI UIDB/00709/2020 research unit, POCI-01-0145-FEDER-022122 research unit PPBI-Portuguese Platform of BioImaging, and to the Portuguese NMR Network (ROTEIRO/0031/2013-PINFRA/22161/2016), through national funds and, where applicable, co-financed by the FEDER through COMPETE 2020, POCI, PORL and PIDDAC. Tiago Santos acknowledges Fundação para a Ciência e Tecnologia (FCT) for the doctoral fellowship PD/BD/142851/2018 integrated in the Ph.D. Programme in NMR applied to chemistry, materials and biosciences (PD/00065/2013) co-financed by Fundo Social Europeu. André Miranda acknowledges to the research fellowship "Rede Nacional de Ressonância Magnética Nuclear" ref. PINFRA/22161/2016-B4 funded by "Programa Operacional Competitividade e

Internacionalização", "Programa Operacional Regional de Lisboa", FEDER, and FCT. C. Cruz acknowledges the grant from FCT ref. UIDP/00709/2020. The authors thank A. Paulo and M. P. Campello for the synthesis and supply of compound C_8.

References

[1] T. Santos, G.F. Salgado, E.J. Cabrita, C. Cruz, G-Quadruplexes and Their Ligands: Biophysical Methods to Unravel G-Quadruplex/Ligand Interactions, Pharmaceuticals. 14 (2021) 769. https://doi.org/10.3390/ph14080769.

[2] K. Lyu, E.Y.C. Chow, X. Mou, T.F. Chan, C.K. Kwok, RNA G-quadruplexes (rG4s): Genomics and biological functions, Nucleic Acids Res. 49 (2021) 5426–5450. https://doi.org/10.1093/nar/gkab187.

[3] L.R. Ganser, M.L. Kelly, D. Herschlag, H.M. Al-Hashimi, The roles of structural dynamics in the cellular functions of RNAs, Nat. Rev. Mol. Cell Biol. 20 (2019) 474–489. https://doi.org/10.1038/s41580-019-0136-0.

[4] M.T. Banco, A.R. Ferré-D'Amaré, The emerging structural complexity of G-quadruplex RNAs, Rna. 27 (2021) 390–402. https://doi.org/10.1261/rna.078238.120.

[5] M.M. Fay, S.M. Lyons, P. Ivanov, RNA G-Quadruplexes in Biology: Principles and Molecular Mechanisms, J. Mol. Biol. 429 (2017) 2127–2147. https://doi.org/10.1016/j.jmb.2017.05.017.

[6] M. Tassinari, S.N. Richter, P. Gandellini, Biological relevance and therapeutic potential of G-quadruplex structures in the human noncoding transcriptome, Nucleic Acids Res. 49 (2021) 3617–3633. https://doi.org/10.1093/nar/gkab127.

[7] C.K. Kwok, A.B. Sahakyan, S. Balasubramanian, Structural Analysis using SHALiPE

to Reveal RNA G-Quadruplex Formation in Human Precursor MicroRNA, Angew. Chemie - Int. Ed. 55 (2016) 8958–8961. https://doi.org/10.1002/anie.201603562.

[8] G. Mirihana Arachchilage, A.C. Dassanayake, S. Basu, A potassium ion-dependent RNA structural switch regulates human pre-miRNA 92b maturation, Chem. Biol. 22 (2015) 262–272. https://doi.org/10.1016/j.chembiol.2014.12.013.

[9] G. Liu, W. Du, H. Xu, Q. Sun, D. Tang, S. Zou, Y. Zhang, M. Ma, G. Zhang, X. Du, S. Ju, W. Cheng, Y. Tian, X. Fu, RNA G-quadruplex regulates microRNA-26a biogenesis and function, J. Hepatol. 73 (2020) 371–382. https://doi.org/10.1016/j.jhep.2020.02.032.

[10] J.A. Imperatore, M.L. Then, K.B. McDougal, M.R. Mihailescu, Characterization of a G-Quadruplex Structure in Pre-miRNA-1229 and in Its Alzheimer's Disease-Associated Variant rs2291418: Implications for miRNA-1229 Maturation, Int. J. Mol. Sci. 2020, Vol. 21, Page 767. 21 (2020) 767. https://doi.org/10.3390/IJMS21030767.

[11] T. Santos, P. Pereira, M.P.C. Campello, A. Paulo, J.A. Queiroz, E. Cabrita, C. Cruz, RNA G-quadruplex as supramolecular carrier for cancer-selective delivery, Eur. J. Pharm. Biopharm. 142 (2019) 473–479. https://doi.org/10.1016/j.ejpb.2019.07.017.

[12] T. Santos, A. Miranda, M.P.C. Campello, A. Paulo, G. Salgado, E.J. Cabrita, C. Cruz, Recognition of nucleolin through interaction with RNA G-quadruplex, Biochem. Pharmacol. (2020) 114208. https://doi.org/10.1016/j.bcp.2020.114208.

[13] K.L. Chan, B. Peng, M.I. Umar, C.-Y. Chan, A.B. Sahakyan, M.T.N. Le, C.K. Kwok, Structural analysis reveals the formation and role of RNA G-quadruplex structures in human mature microRNAs, Chem. Commun. 54 (2018) 10878–10881. https://doi.org/10.1039/C8CC04635B.

[14] W. Tan, L. Yi, Z. Zhu, L. Zhang, J. Zhou, G. Yuan, Hsa-miR-1587 G-quadruplex formation and dimerization induced by NH4+, molecular crowding environment and jatrorrhizine derivatives, Talanta. 179 (2018) 337–343. https://doi.org/10.1016/j.talanta.2017.11.041.

[15] W. Tan, J. Zhou, J. Gu, M. Xu, X. Xu, G. Yuan, Probing the G-quadruplex from hsa-miR-3620-5p and inhibition of its interaction with the target sequence, Talanta. 154 (2016) 560–566. https://doi.org/10.1016/j.talanta.2016.02.037.

[16] S. Pandey, P. Agarwala, G.G. Jayaraj, R. Gargallo, S. Maiti, The RNA Stem-Loop to G-Quadruplex Equilibrium Controls Mature MicroRNA Production inside the Cell, Biochemistry. (2015). https://doi.org/10.1021/acs.biochem.5b00574.

[17] N. Koralewska, A. Szczepanska, K. Ciechanowska, M. Wojnicka, M. Pokornowska, M.C. Milewski, D. Gudanis, D. Baranowski, C. Nithin, J.M. Bujnicki, Z. Gdaniec, M. Figlerowicz, A. Kurzynska-Kokorniak, RNA and DNA G-quadruplexes bind to human dicer and inhibit its activity, Cell. Mol. Life Sci. 78 (2021) 3709–3724. https://doi.org/10.1007/s00018-021-03795-w.

[18] D. Barh, R. Malhotra, B. Ravi, P. Sindhurani, MicroRNA let-7: An emerging next-generation cancer therapeutic, Curr. Oncol. (2010). https://doi.org/10.3747/co.v17i1.356.

[19] W.Y. Zhu, B. Luo, J.Y. An, J.Y. He, D.D. Chen, L.Y. Xu, Y.Y. Huang, X.G. Liu, H.B. Le, Y.K. Zhang, Differential expression of miR-125a-5p and let-7e predicts the progression and prognosis of non-small cell lung cancer, Cancer Invest. 32 (2014) 394–401. https://doi.org/10.3109/07357907.2014.922569.

[20] E. Chirshev, K.C. Oberg, Y.J. Ioffe, J.J. Unternaehrer, Let - 7 as biomarker, prognostic indicator, and therapy for precision medicine in cancer, Clin. Transl. Med. 8 (2019) 24.

https://doi.org/10.1186/s40169-019-0240-y.

[21] B. Boyerinas, S.M. Park, A. Hau, A.E. Murmann, M.E. Peter, The role of let-7 in cell differentiation and cancer, Endocr. Relat. Cancer. 17 (2010) 19–36. https://doi.org/10.1677/ERC-09-0184.

[22] M. Xiao, J. Cai, L. Cai, J. Jia, L. Xie, Y. Zhu, B. Huang, D. Jin, Z. Wang, Let-7e sensitizes epithelial ovarian cancer to cisplatin through repressing DNA double strand break repair, J. Ovarian Res. 10 (2017) 24. https://doi.org/10.1186/s13048-017-0321-8.

[23] J. Figueiredo, T. Santos, A. Miranda, D. Alexandre, B. Teixeira, P. Simões, J. Lopes-Nunes, C. Cruz, Ligands as Stabilizers of G-Quadruplexes in Non-Coding RNAs, Molecules. 26 (2021) 6164. https://doi.org/10.3390/molecules26206164.

[24] A. Henn, A. Joachimi, D.P.N. Gonçalves, D. Monchaud, M.P. Teulade-Fichou, J.K.M. Sanders, J.S. Hartig, Inhibition of dicing of guanosine-rich shRNAs by quadruplex-binding compounds., Chembiochem. 9 (2008) 2722–2729. https://doi.org/10.1002/cbic.200800271.

[25] A. Bugaut, P. Murat, S. Balasubramanian, An RNA hairpin to g-quadruplex conformational transition, J. Am. Chem. Soc. (2012). https://doi.org/10.1021/ja308665g.

[26] B.F. Pickering, D. Yu, M.W. Van Dyke, Nucleolin protein interacts with microprocessor complex to affect biogenesis of microRNAs 15a and 16, J. Biol. Chem. 286 (2011) 44095–44103. https://doi.org/10.1074/jbc.M111.265439.

[27] W. Jia, Z. Yao, J. Zhao, Q. Guan, L. Gao, New perspectives of physiological and pathological functions of nucleolin (NCL), Life Sci. 186 (2017) 1–10. https://doi.org/10.1016/j.lfs.2017.07.025.

[28] I. Ugrinova, M. Petrova, M. Chalabi-Dchar, P. Bouvet, Multifaceted Nucleolin Protein and Its Molecular Partners in Oncogenesis, in: Adv. Protein Chem. Struct. Biol., 2018: pp. 133–164. https://doi.org/10.1016/bs.apcsb.2017.08.001.

[29] S. Lago, E. Tosoni, M. Nadai, M. Palumbo, S.N. Richter, The cellular protein nucleolin preferentially binds long-looped G-quadruplex nucleic acids, Biochim. Biophys. Acta - Gen. Subj. 1861 (2017) 1371–1381. https://doi.org/10.1016/j.bbagen.2016.11.036.

[30] E. Pereira, L. Do Quental, E. Palma, M.C. Oliveira, F. Mendes, P. Raposinho, I. Correia, J. Lavrado, S. Di Maria, A. Belchior, P. Vaz, I. Santos, A. Paulo, Evaluation of Acridine Orange Derivatives as DNA-Targeted Radiopharmaceuticals for Auger Therapy: Influence of the Radionuclide and Distance to DNA, Sci. Rep. 7 (2017) 42544. https://doi.org/10.1038/srep42544.

[31] S.Y. Yang, P. Lejault, S. Chevrier, R. Boidot, A.G. Robertson, J.M.Y. Wong, D. Monchaud, Transcriptome-wide identification of transient RNA G-quadruplexes in human cells, Nat. Commun. 9 (2018) 4730. https://doi.org/10.1038/s41467-018-07224-8.

[32] A. De Cian, E. DeLemos, J.L. Mergny, M.P. Teulade-Fichou, D. Monchaud, Highly efficient G-quadruplex recognition by bisquinolinium compounds, J. Am. Chem. Soc. 129 (2007) 1856–1857. https://doi.org/10.1021/ja067352b.

[33] R. Rodriguez, S. Müller, J.A. Yeoman, C. Trentesaux, J.F. Riou, S. Balasubramanian, A novel small molecule that alters shelterin integrity and triggers a DNA-damage response at telomeres, J. Am. Chem. Soc. 130 (2008) 15758–15759. https://doi.org/10.1021/ja805615w.

[34] M. Di Antonio, G. Biffi, A. Mariani, E.A. Raiber, R. Rodriguez, S. Balasubramanian, Selective RNA versus DNA G-quadruplex targeting by situ click chemistry, Angew.

Chemie - Int. Ed. 51 (2012) 11073–11078. https://doi.org/10.1002/anie.201206281.

[35] M. Read, R.J. Harrison, B. Romagnoli, F.A. Tanious, S.H. Gowan, A.P. Reszka, W.D. Wilson, L.R. Kelland, S. Neidle, Structure-based design of selective and potent G quadruplex-mediated telomerase inhibitors, Proc. Natl. Acad. Sci. U. S. A. 98 (2001) 4844–4849. https://doi.org/10.1073/pnas.081560598.

[36] F.X. Han, R.T. Wheelhouse, L.H. Hurley, Interactions of TMPyP4 and TMPyP2 with quadruplex DNA. Structural basis for the differential effects on telomerase inhibition, J. Am. Chem. Soc. 121 (1999) 3561–3570. https://doi.org/10.1021/ja984153m.

[37] G. Pennarun, C. Granotier, L.R. Gauthier, D. Gomez, F. Hoffschir, E. Mandine, J.F. Riou, J.L. Mergny, P. Mailliet, F.D. Boussin, Apoptosis related to telomere instability and cell cycle alterations in human glioma cells treated by new highly selective G-quadruplex ligands, Oncogene. 24 (2005) 2917–2928. https://doi.org/10.1038/sj.onc.1208468.

[38] J.-L. Mergny, Thermal difference spectra: a specific signature for nucleic acid structures, Nucleic Acids Res. 33 (2005) e138–e138. https://doi.org/10.1093/nar/gni134.

[39] M. Webba da Silva, NMR methods for studying quadruplex nucleic acids, Methods. 43 (2007) 264–277. https://doi.org/10.1016/j.ymeth.2007.05.007.

[40] I. Renard, M. Grandmougin, A. Roux, S.Y. Yang, P. Lejault, M. Pirrotta, J.M.Y. Wong, D. Monchaud, Small-molecule affinity capture of DNA/RNA quadruplexes and their identification in vitro and in vivo through the G4RP protocol, Nucleic Acids Res. 47 (2019) 502–510. https://doi.org/10.1093/nar/gkz215.

[41] S. Haldar, Y. Zhang, Y. Xia, B. Islam, S. Liu, F.L. Gervasio, A.J. Mulholland, Z.A.E.

Waller, D. Wei, S. Haider, Ligand-induced unfolding mechanism of an RNA G-quadruplex, BioRxiv. (2021) 2021.10.26.465985. https://doi.org/10.1101/2021.10.26.465985.

[42] J. Mitteaux, P. Lejault, F. Wojciechowski, A. Joubert, J. Boudon, N. Desbois, C.P. Gros, R.H.E. Hudson, J.B. Boulé, A. Granzhan, D. Monchaud, Identifying G-Quadruplex-DNA-Disrupting Small Molecules, J. Am. Chem. Soc. 143 (2021) 12567–12577. https://doi.org/10.1021/jacs.1c04426.

[43] P. Lejault, J. Mitteaux, F.R. Sperti, D. Monchaud, How to untie G-quadruplex knots and why?, Cell Chem. Biol. 28 (2021) 436–455. https://doi.org/10.1016/j.chembiol.2021.01.015.

[44] A. Kerkour, J.L. Mergny, G.F. Salgado, NMR based model of human telomeric repeat G-quadruplex in complex with 2,4,6-triarylpyridine family ligand, Biochim. Biophys. Acta - Gen. Subj. 1861 (2017) 1293–1302. https://doi.org/10.1016/j.bbagen.2016.12.016.

[45] L.P.P. Patro, A. Kumar, N. Kolimi, T. Rathinavelan, 3D-NuS: A Web Server for Automated Modeling and Visualization of Non-Canonical 3-Dimensional Nucleic Acid Structures, J. Mol. Biol. 429 (2017) 2438–2448. https://doi.org/10.1016/j.jmb.2017.06.013.

[46] P. Stadlbauer, B. Islam, M. Otyepka, J. Chen, D. Monchaud, J. Zhou, J.L. Mergny, J. Šponer, Insights into G-Quadruplex-Hemin Dynamics Using Atomistic Simulations: Implications for Reactivity and Folding, J. Chem. Theory Comput. 17 (2021) 1883–1899. https://doi.org/10.1021/acs.jctc.0c01176.

[47] A. Miranda, T. Santos, J. Carvalho, D. Alexandre, A. Jardim, C.R.F. Caneira, V. Vaz, B. Pereira, R. Godinho, D. Brito, V. Chu, J.P. Conde, C. Cruz, Aptamer-based

approaches to detect nucleolin in prostate cancer, Talanta. 226 (2021) 122037. https://doi.org/10.1016/j.talanta.2020.122037.

[48] J. Balzeau, M.R. Menezes, S. Cao, J.P. Hagan, The LIN28/let-7 pathway in cancer, Front. Genet. 8 (2017) 31. https://doi.org/10.3389/fgene.2017.00031.

[49] L. Pandolfini, I. Barbieri, A.J. Bannister, A. Hendrick, B. Andrews, N. Webster, P. Murat, P. Mach, R. Brandi, S.C. Robson, V. Migliori, A. Alendar, M. d'Onofrio, S. Balasubramanian, T. Kouzarides, METTL1 Promotes let-7 MicroRNA Processing via m7G Methylation, Mol. Cell. 74 (2019) 1278-1290.e9. https://doi.org/10.1016/j.molcel.2019.03.040.

[50] S. Manaye, R. Eritja, A. Aviñó, J. Jaumot, R. Gargallo, Porphyrin binding mechanism is altered by protonation at the loops in G-quadruplex DNA formed near the transcriptional activation site of the human c-kit gene, Biochim. Biophys. Acta - Gen. Subj. 1820 (2012) 1987–1996. https://doi.org/10.1016/j.bbagen.2012.09.006.

[51] S.T.D. Hsu, P. Varnai, A. Bugaut, A.P. Reszka, S. Neidle, S. Balasubramanian, A G-rich sequence within the c-kit oncogene promoter forms a parallel G-quadruplex having asymmetric G-tetrad dynamics, J. Am. Chem. Soc. 131 (2009) 13399–13409. https://doi.org/10.1021/ja904007p.

[52] M. Małgowska, D. Gudanis, A. Teubert, G. Dominiak, Z. Gdaniec, How to study G-quadruplex structures, Biotechnologia. 93 (2013) 381–390. https://doi.org/10.5114/bta.2012.46592.

[53] K. Wang, D.P. Flaherty, L. Chen, D. Yang, High-Throughput Screening of G-Quadruplex Ligands by FRET Assay, in: Methods Mol. Biol., 2019: pp. 323–331. https://doi.org/10.1007/978-1-4939-9666-7_19.

[54] M. Saad, A. Guédin, S. Amor, A. Bedrat, N.J. Tourasse, H. Fayyad-Kazan, G. Pratviel, L. Lacroix, J.L. Mergny, Mapping and characterization of G-quadruplexes in the genome of the social amoeba Dictyostelium discoideum, Nucleic Acids Res. 47 (2019) 4363–4374. https://doi.org/10.1093/nar/gkz196.

[55] A. San, D. Palmieri, A. Saxena, S. Singh, In silico study predicts a key role of RNA-binding domains 3 and 4 in nucleolin-miRNA interactions, BioRxiv. (2021) 2021.06.09.447752. https://doi.org/10.1101/2021.06.09.447752.

[56] V. González, K. Guo, L. Hurley, D. Sun, Identification and characterization of nucleolin as a c-myc G-quadruplex-binding protein, J. Biol. Chem. 284 (2009) 23622–23635. https://doi.org/10.1074/jbc.M109.018028.

[57] M. Zacchia, M.L. Abategiovanni, S. Stratigis, G. Capasso, Potassium: From Physiology to Clinical Implications, Kidney Dis. 2 (2016) 72–79. https://doi.org/10.1159/000446268.

[58] T. Santos, A. Miranda, L. Imbert, A. Jardim, C.R.F. Caneira, V. Chu, J.P. Conde, M.P.C. Campello, A. Paulo, G. Salgado, E.J. Cabrita, C. Cruz, Pre-miRNA-149 G-quadruplex as a molecular agent to capture nucleolin, Eur. J. Pharm. Sci. 169 (2022) 106093. https://doi.org/10.1016/J.EJPS.2021.106093.